Single-mode dynamics of the Rayleigh-Taylor instability at any density ratio

P. Ramaprabhu and Guy Dimonte
Los Alamos National Laboratory, Los Alamos, New Mexico 87545, USA
(Received 14 September 2004; revised manuscript received 1 February 2005; published 30 March 2005)

The behavior of a periodic array of Rayleigh-Taylor bubbles (and spikes) of wavelength λ is investigated at different density ratios using three-dimensional numerical simulations. The scaled bubble and spike velocities ($v_{b,s}/\sqrt{Ag\lambda/2}$), are found to vary with the Atwood number A, and are compared with recent potential flow theories. Simulations at different grid resolutions reveal that the convergence rates of bubble velocities improve with increasing A, while the converse holds true for spike velocities. The asymptotic radius of curvature at the bubble tip is found to be independent of A, consistent with potential flow theory. These results are useful in validating potential flow theory models of the nonlinear stage of the Rayleigh-Taylor instability.

DOI: 10.1103/PhysRevE.71.036314 PACS number(s): 47.20.Bp

I. INTRODUCTION

The interface between two fluids of different densities ($\rho_1 > \rho_2$) is unstable if the light fluid pushes against the heavy [Rayleigh-Taylor (RT) instability [1,2]]. Such instabilities have been observed in type II supernovae [3], and in the inertial confinement fusion process [4], where the RT-driven mixing reduces the thermonuclear yield. Infinitesimal perturbations imposed at the interface grow exponentially in time [5] according to

$$h = h_0 \cosh(\Gamma t). \tag{1}$$

At large amplitudes, the light fluid penetrates the heavy in the form of *bubbles* with a constant terminal velocity, while fingers of the heavy fluid form *spikes*. For small density differences, the flow is symmetric with respect to the bubble and spike penetration. This symmetry is broken at higher Atwood numbers [$A=(\rho_1-\rho_2)/(\rho_1+\rho_2)$], as spikes grow faster than bubbles, ultimately approaching free fall ($h_s \sim t^2$) at infinite density ratios.

When a spectrum of wavelengths is present, the resulting flow is chaotic, and evolves through interactions between bubbles (spikes) of different sizes. These modal interactions may involve the merger of two bubbles to form a larger structure [6,7], or the sampling of successively longer wavelengths from the modes present in the initial conditions [8]. Such phenomena are often described by modeling single-bubble behavior and bubble-bubble interactions in the nonlinear stage. Furthermore, models that characterize the role of the initial conditions on the turbulent RT flow [8,9] also rely on single-mode dynamics in the nonlinear stage, to develop a picture of the turbulent RT flow. However, such efforts depend critically on the knowledge of single-mode bubble terminal velocities as a function of the Atwood number [8]. In this paper, we report results from numerical simulations of the linear and nonlinear stages of RT evolution. We review three recently proposed potential flow models of the RT bubble, and conclude that our results compare favorably with the model of Goncharov [17].

Davies and Taylor [10] were the first to propose a potential flow theory approach to describe single-mode bubble behavior in the nonlinear regime. Layzer [11] suggested a similar potential flow model to describe the flow around the bubble tip for a fluid-vacuum interface ($A=1$). He considered cylindrical bubbles in three dimensions (3D), represented by a Bessel function for the velocity potential. Then the Bernoulli equations are applied to the bubble tip, to yield ordinary differential equations for the position, velocity, and radius of curvature of the bubble. Analytical solutions to these equations were provided recently by Mikaelian [12]. The asymptotic bubble velocity from such models is

$$V_b = C\sqrt{g\lambda}, \tag{2}$$

where g is the acceleration, λ is the wavelength, and C was determined to be ~0.5 from experiments [10,13]. Zhang [14] extended Layzer's model to RT spikes at $A=1$. Hecht, Alon, and Shvarts [15] applied a similar analysis to other flow situations including bubble evolution through a layer of finite thickness (2D), two-bubble competition (2D), and a 3D bubble in a rectangular geometry. They also argued that to second order, a square mode has the same growth rate as a cylindrical mode. The 3D simulations of Hecht *et al.* [16] also obtain similar penetration distances for square and cylindrical modes to within numerical accuracy. Thus, our results below for a square periodic array are valid for a flow initialized with a Bessel function J_0 for the density profile.

More recently, Goncharov [17] and Sohn [18] have extended such models to arbitrary density ratios. The models apply potential theory to the flow around the bubble tip, and converge to Layzer's approximation in the limit of $A=1$. Goncharov uses a Bessel function for the velocity potentials of the heavy and light fluids, and finds in the asymptotic limit that the bubble velocity is given by

$$v_b = 1.02\sqrt{\frac{2A}{1+A}\frac{g}{k}}. \tag{3}$$

Sohn, who uses a different form of the potential function (discussed in Sec. III) for the light fluid, obtains

$$v_b \sim \sqrt{\frac{AgR}{\beta_1}}, \tag{4}$$

where β_1 represents the first zero of the Bessel function, R is the tube radius, and may be related to the wave number using

$\beta_1/R \sim k$. For lower density ratios, the two models diverge, until the ratio of the Froude numbers from Sohn's model to Goncharov's model is 1:1.4 at $A=0$. The steady-state bubble velocity may also be obtained by equating the buoyancy and drag forces experienced by a rising 3D bubble. Interestingly, drag-buoyancy models such as those proposed by Alon *et al.* [19] and Oron *et al.* [20] agree with Eq. (3). Note that while the Froude number associated with a RT bubble has been defined in several ways, we adopt the physically intuitive definition of Scorer [21] and Alon *et al.* [19]

$$v_b = \mathrm{Fr}\sqrt{\frac{\delta\rho}{\rho} g \frac{D_b}{2}}. \tag{5}$$

Defined this way, the Froude number may be interpreted as a ratio of terms in the steady-state drag-buoyancy equation, and will be later shown to be independent of the Atwood number.

We also compare our results with a recent model proposed by Abarzhi, Nishihara, and Glimm [22] who employ a multiple harmonic analysis to explore the shape of the bubble at late time (Goncharov, who also uses a similar analysis, reports that the amplitudes of higher harmonic terms used to describe the bubble front vanish rapidly). However, the central difference between the Goncharov-type models (including the models of Sohn and Layzer), and the approach adopted by Abarzhi *et al.* is that the latter forces the flow to satisfy boundary conditions at $\pm\infty$ along the direction of gravity. Goncharov's analysis, on the other hand, is valid near the bubble tip: his choice of potential function includes a source term for mass at negative infinity, to satisfy the zero-mass-flux condition across the interface. Abarzhi *et al.*'s terminal velocity (and bubble curvature ζ) differs from Goncharov's at low Atwood numbers. While the expressions for the exact solutions will not be reproduced here, they may be obtained by solving the following set of equations for ζ and v_b [22]:

$$\left(\frac{\zeta}{k}\right)^4 - \left(\frac{\zeta}{k}\right)^3 \frac{1}{A} + \frac{9}{32}\left(\frac{\zeta}{k}\right)^2 - \left(\frac{3}{16}\right)^3 = 0, \tag{6}$$

$$v_b = \sqrt{g/k}\left(\frac{8|\zeta|}{k}\right)^{3/2}. \tag{7}$$

In this paper, we test the above models using 3D numerical simulations of a square periodic array of RT bubbles, at different grid resolutions. Section II contains a description of the numerical technique used, and the computational setup. The results are presented in Sec. III, while Sec. IV contains a discussion and summary of our findings.

II. NUMERICS

A 3D, third-order accurate, finite volume Eulerian solver was used for the numerical calculations. The algorithm and numerical techniques are described in detail in [23]. Some essential features are reviewed herein. Numerical dissipation provides an artificial viscosity that smooths out sharp gradients characteristic of Euler equation solutions. The van Leer technique [24] was used to determine the convective fluxes, thus preventing spurious overshoots and undershoots associated with higher order numerical schemes. A Poisson equation for pressure correction is solved at every time step to enforce global mass conservation to within a tolerance of 10^{-5}. This algorithm belongs to the class of techniques commonly referred to as monotone integrated large eddy simulations (MILES), and has been demonstrated to be effective in the simulation of flows with shocks and discontuinities such as RT and Richtmyer-Meshkov instabilities [25].

Periodic boundary conditions in the lateral directions, and zero-flux conditions in the vertical direction were employed. The perturbations were initialized as cosine waves of the density surface:

$$h_0(x,y) = a_0\left\{\cos\left(\frac{2\pi x}{\lambda}\right) + \cos\left(\frac{2\pi y}{\lambda}\right)\right\}. \tag{8}$$

This form of the perturbation places the bubble at the center of the box, while the spikes appear at the four corners. The wavelength of the perturbation was set to 10 cm, while the amplitude a_0 was 0.1 cm to ensure that the modes are well within the nonlinear saturation threshold ($h_{\mathrm{nl}}k \sim 1$). To test the effect of zoning, the calculations were performed at grid resolutions of $\lambda/\Delta = 4$, 8, 16, 32, and 64 where Δ is the zone width. The size of the computational domain was $10\times 10 \times 40$ cm^3 in the x, y, and z directions, respectively (here, z is the direction of the gravity vector). The simulations had Atwood numbers of 0.005, 0.1, 0.25, 0.5, 0.75, 0.9, and 1. The acceleration was set to 2 cm/s^2.

III. RESULTS

Figures 1(a), 1(b), and 1(c) show the isosurfaces of 50% volume fraction at late times for $A=0.1$, 0.5, and 0.9, respectively. Spikes form at the corners of the computational domain, and are shown in a diagonal cross section for these simulations in Figs. 1(d), 1(e), and 1(f). The simulations were performed at a resolution of $32\times 32\times 128$ zones. Bubbles and spikes show greater symmetry at lower density differences [Figs. 1(d) and 1(e)], while spikes outpace bubble growth at $A=0.9$ Fig. 1(f). The lower Atwood number cases show more vorticity in general, evidenced by the formation of Kelvin-Helmholtz type roll-ups on the spike surfaces. The times represented in Fig. 1 were chosen such that the bubble penetration in each of the cases is roughly the same, i.e., $h_b/\lambda \sim 0.8$.

The corresponding bubble amplitude h_b [shown on a semilogarithmic plot in Fig. 2(a)] was deduced by tracking the bubble tip. The bubble amplitude h_b (in centimeters), shows a region of exponential growth ($t<4$ s), followed by saturation of the bubble velocity [Fig. 2(b)]. The bubble amplitude from Eq. (1) is shown as the solid line in Fig. 2(a), and is in good agreement with our simulations for $t<4$ s. The Froude number and the scaled bubble velocity were then inferred from fitting a straight line to $\partial h_b/\partial t$ in Fig. 2(b) at late times.

At a resolution of 64 zones/λ, a numerical instability at the bubble tip was observed for $A>0.75$. The bubbles which occupy much of the computational domain at these density

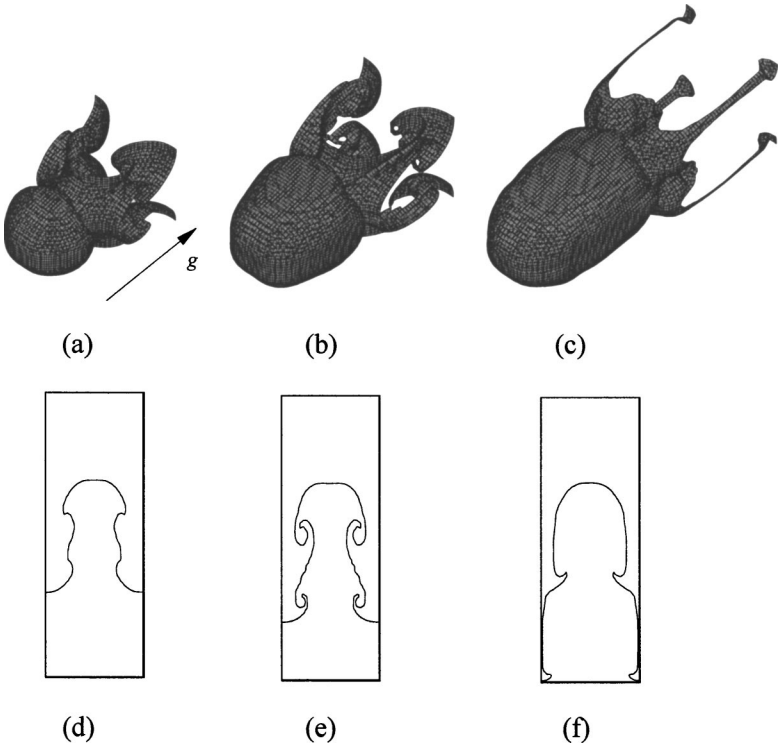

FIG. 1. Evolution of a single-mode RT bubble for $A=0.1$ (a), 0.5 (b), and 0.9 (c). The spike cross sections in a diagonal plane are shown in (d), (e), and (f) for the same cases. The times shown are such that $h_b \sim 0.8\lambda$ for each case.

ratios are over-resolved. Consequently, secondary ridges form at the bubble front at late times. This instability is not unlike that observed by Li [26], at $A=0.905$ and near the incompressible limit. The instability observed here disappears with the addition of a small viscosity that damps the artificial secondary modes. This viscosity was chosen to match the numerical dissipation from the 32 zones/λ case which remained stable even at high Atwood numbers. The numerical viscosity may be determined from the scaling [27,28]

$$\nu = \varpi \sqrt{Ag\Delta^3}, \tag{9}$$

where the coefficient ϖ was obtained by fitting the numerical solution to the classical growth rates in the linear stage as described below.

Indeed, the scaling relation (9) may be directly verified using our simulations. The exponential growth rate Γ normalized by the inviscid classical growth rate $\sqrt{Akg}$ is shown in Fig. 3(a) for different Atwood numbers. The growth rate approaches ~95% of its inviscid value at $k\Delta \sim 0.098$ (corresponding to 64 zones/λ). Γ is modified in the presence of viscosity according to the dispersion relation given by Chandrasekhar [5]. Solving the dispersion equation to fit the numerically obtained growth rates, we may infer an effective numerical viscosity ν and hence ϖ from Eq. (9). The result, shown in Fig. 3(b) for different zoning, is independent of A, and corresponds to $\varpi = 0.33 \pm 0.09$, thus validating Eq. (9). The 64 zones/λ case exhibits higher values of ϖ, because the convergence rate drops at higher resolutions, indicating

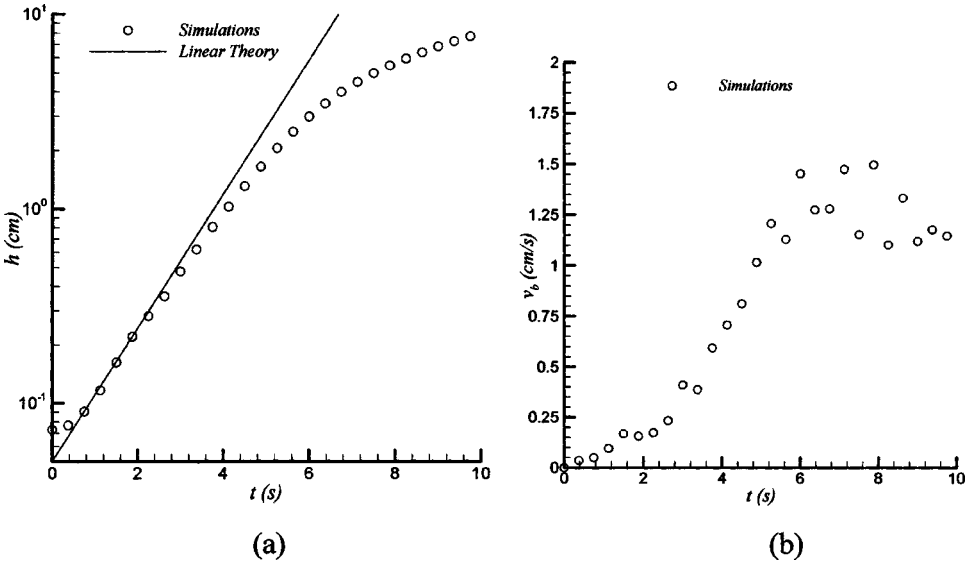

FIG. 2. Time trace of bubble amplitude h_b (a) and velocity v_b (b) for RT evolution with $A=0.5$.

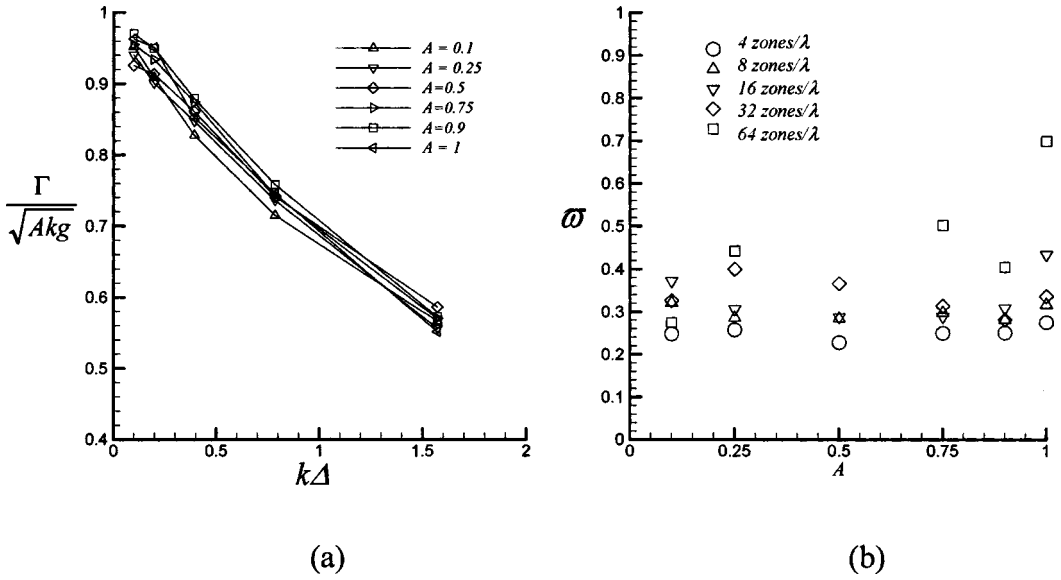

FIG. 3. (a) Convergence of the growth rate Γ at different Atwood numbers and (b) the nondimensional viscosity coefficient ϖ at different zoning.

that it may not be possible to achieve the theoretical convergence rate as $k\Delta \to 0$.

The amplitude at which a mode transitions from exponential growth (1) to nonlinear evolution given by Eq. (3) may be inferred by determining the time at which the linear and nonlinear modal velocities become the same. This procedure, attributed to Fermi by Layzer [11], is often used in modeling the role of initial conditions in the late-time dynamics [8,9]. Thus, we may obtain t_{nl} from the following:

$$v_b = \Gamma h_{\mathrm{nl}} = \frac{h_0 \Gamma}{2} \exp(\Gamma t_{\mathrm{nl}}). \tag{10}$$

Then, the transition amplitude h_{nl} is determined trivially by combining Eqs. (1) and (10). Figure 4 shows $h_{\mathrm{nl}}k$ as a function of A, and is a comparison of theoretical [Γ determined from Eq. (1) and v_b from models] and numerical (Γ and v_b obtained directly from simulations) values. $h_{\mathrm{nl}}k$ from the simulations shows excellent agreement with the Goncharov model. The lower Atwood number cases experience a longer linear growth stage, and a delayed transition to nonlinearity due to smaller values of Γ. Furthermore, the bubbles stay linear up to higher amplitudes for the low Atwood number cases. This may be because at low density ratios, the shape of the interface stays approximately sinusoidal even at higher amplitudes. In contrast, the high Atwood number cases soon resemble a square wave, thus possibly deviating from the classical growth rate. The transition time t_{nl} was used in determining h_b for Fig. 1 so that

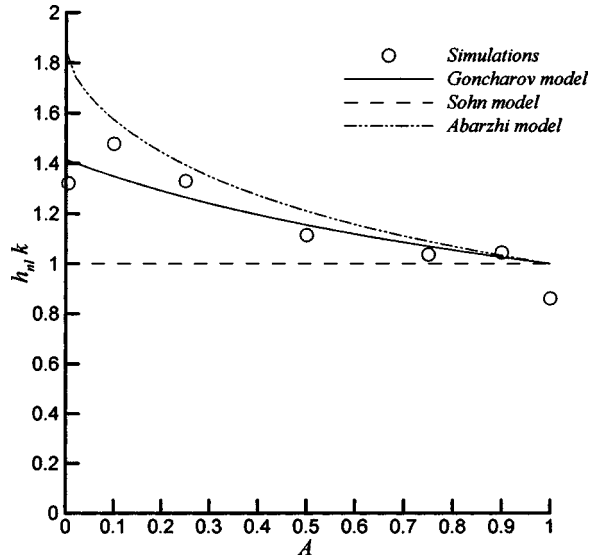

FIG. 4. Nonlinear saturation amplitudes $h_{\mathrm{nl}}k$ from simulations and theory as a function of A.

$$h_b = v_b(t - t_{\mathrm{nl}}) + h_0 \cosh(\Gamma t_{\mathrm{nl}}) = 0.8\lambda_b, \tag{11}$$

where v_b was chosen according to Eq. (3), since Goncharov's model gives the best agreement in Fig. 4.

At $A=1$, we can easily show from the following analysis that $h_{\mathrm{nl}}k=1$, as observed in Fig. 4. Using $v_{b,A=1} \sim \sqrt{g/k}$ from the models in Eq. (9), we get

$$t_{\mathrm{nl}} = \frac{1}{\Gamma} \ln\left(\frac{2v_{b,A=1}}{h_0 \Gamma}\right). \tag{12}$$

Thus, the nonlinear transition amplitude at an Atwood number of 1 is given by

$$h_{\mathrm{nl}}k = \frac{h_0}{2} \exp(\Gamma t_{\mathrm{nl}})k = \frac{v_b}{\sqrt{g/k}} = 1 \tag{13}$$

in agreement with our simulations.

Figure 5 shows the asymptotic scaled bubble velocity $v_{\mathrm{scl},b} = v_b/\sqrt{Ag\lambda/2}$ as a function of the Atwood number at different zone widths. The error associated with determining $v_{\mathrm{scl},b}$ was $\sim$10% for these simulations. Sohn's analysis [18] gives $v_b/\sqrt{Ag\lambda/2}$ independent of A, while Goncharov's

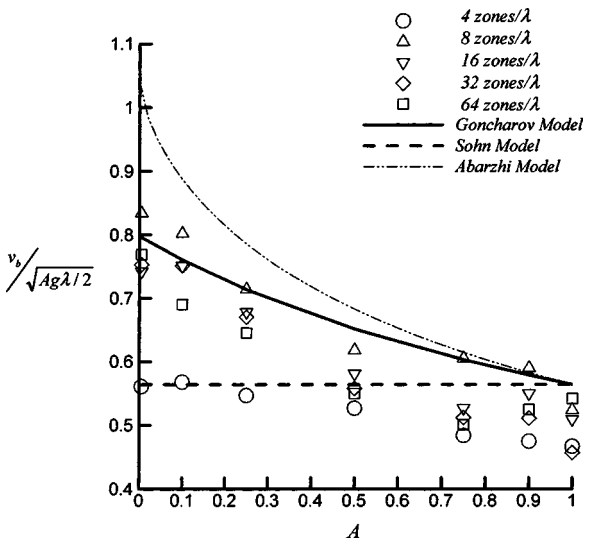

FIG. 5. The scaled bubble ($v_b/\sqrt{Ag\lambda/2}$) velocities as a function of A for different zoning.

equation (19) for a 3D bubble predicts $v_{\mathrm{scl},b}=\sqrt{2/\pi(1+A)}$ [17]. The model suggested by Abarzhi *et al.* [22] is also shown in Fig. 5, and differs from Goncharov's solution at low density ratios. All the models agree with Layzer's solution [11] (and our simulations) at $A=1$, but diverge with decreasing A. For a grid resolution $\geqslant 8$ zones/λ, our simulations show the closest agreement with Goncharov.

We note that Goncharov uses a different form of the potential function from Sohn. In 3D cylindrical geometry, [17] uses for the heavy and light fluid potentials

$$\phi_G^h = a(t)J_0(kr)e^{-kz}, \quad \phi_G^l = b_1(t)J_0(kr)e^{kz} + b_2(t)z \tag{14a}$$

in contrast to Sohn whose choices of velocity potentials were [18]

$$\phi_S^h = a(t)J_0(kr)e^{-kz}, \quad \phi_S^l = -a(t)J_0(kr)e^{-kz}, \tag{14b}$$

if one makes the equivalence $k=\beta_1/R$, where R is the radius of the cylinder, and β_1 is the first zero of J_0. Abarzhi *et al.* [22] point out that (14b) and similar models result in a net mass flux across the interface at $z=0$. This difficulty is solved by Goncharov with the addition of the mass-flux term in (14a). However, this extra source term violates the zero-flux conditions at $z\to-\infty$. As our simulations have shown here, Goncharov's model appears to work well near the bubble tip: Since the flow around the bubble tip determines the bubble terminal velocity, we conclude that (14a) adequately captures the physics in this region of the flow. The violation of boundary conditions at infinity does not seem to affect the solution at the interface, particularly since it is claimed to be valid only near the interface. Mikaelian [12] also obtains Eq. (3) by analytically solving the governing equations for a special value of the initial amplitude $h_0=1/2k$. We also note that a higher approximation of Abarzhi's solution [29] gives better agreement with our simulations and Eq. (3). For $A\to 0$, this higher order solution gives $v_b\sim 1.5\sqrt{Ag/k}$, while the corresponding expression

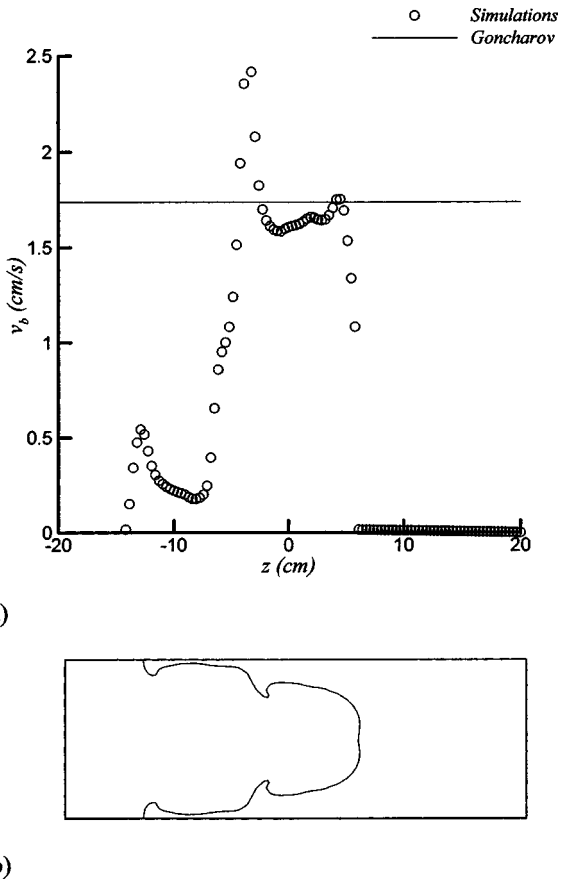

FIG. 6. (a) Comparison of the vertical velocity profile from the simulations and the Goncharov model at $A=0.9$. (b) The $f_l=0.5$ contour in a diagonal plane from the $A=0.9$ simulation, showing the onset of Kelvin-Helmholtz rollups.

from the drag-buoyancy model is $v_b\sim 1.4\sqrt{Ag/k}$.

Figure 6(a) is a comparison of the z profile of the asymptotic vertical velocity associated with the bubble, from simulations and the Goncharov model at $A=0.9$. The asymptotic velocity $v_z(z)$ from the model was inferred using [30]

$$b_1(t) = \frac{\dot{\zeta}_0(k+8\zeta_2)}{k(k-8\zeta_2)}, \quad b_2(t) = \frac{16\dot{\zeta}_0\zeta_2}{(8\zeta_2-k)} \tag{15}$$

in Eq. (14a), where $\dot{\zeta}_0$ is the bubble tip velocity and ζ_2 is the bubble curvature. For $t\to\infty$, $\zeta_2\to -k/8$, giving $b_1\to 0$ and $b_2\to\dot{\zeta}_0=v_b$. Thus at late times, Goncharov predicts that this velocity be constant everywhere within the light fluid. The velocity associated with the light fluid was calculated from our simulations using

$$v_{\mathrm{bulk}}(z) = \frac{\int f_l v_z dA(z)}{\int f_l dA(z)}, \tag{16}$$

where f_l is the fraction by volume of the light fluid. Within the bubble, $v_{\mathrm{bulk}}(z)$ is constant and shows reasonable agree-

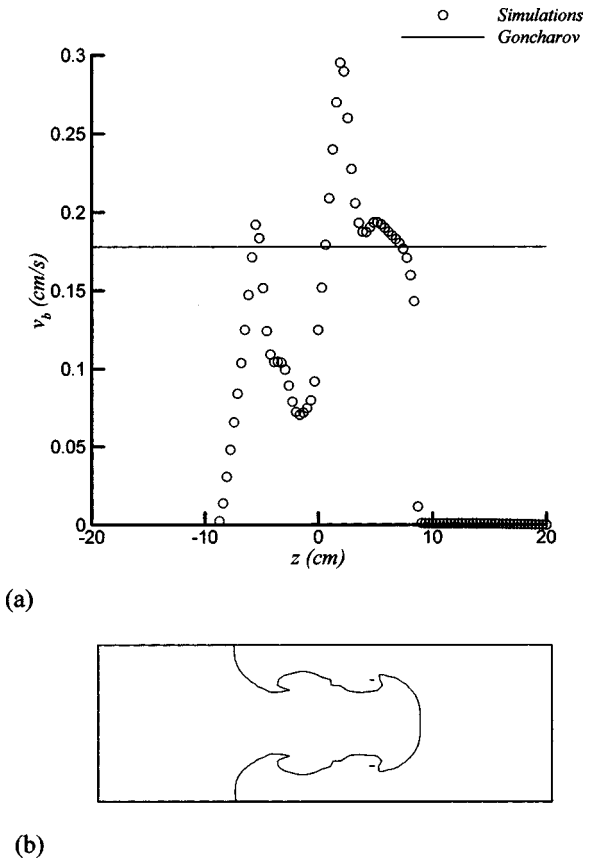

FIG. 7. (a) Comparison of the vertical velocity profile from the simulations and the Goncharov model at $A=0.005$. (b) The $f_l=0.5$ contour in a diagonal plane from the $A=0.005$ simulation, showing the onset of Kelvin-Helmholtz rollups.

ment with b_2 from Eqs. (14) and (15). The peaks of $v_{\mathrm{bulk}}(z)$ from the simulations correspond closely to kinks on the bubble surface [Fig. 6(b)], indicating the onset of Kelvin-Helmholtz rollups.

This effect is more pronounced at low A [Figs. 7(a) and 7(b)], where the bubble cross section shows greater variations. From mass conservation, we expect the flow to accelerate as it enters a narrower section and vice versa. This is confirmed by the locations of peaks and valleys of $v_{\mathrm{bulk}}(z)$ in Fig. 7(a), which are in good correlation with the features in Fig. 7(b). To obtain the true bulk velocity driving a bubble, $v_{\mathrm{bulk}}(z)$ is averaged along z between points where the velocity is 50% of the peak. The results from this procedure at different Atwood numbers are compared with Eq. (3) in Fig. 8, and show good agreement. Thus, the presence of vortices may modify the local velocities, but not the bulk motion driving the bubble, which remains in agreement with the potential flow approximation.

It is easy to gain physical insight into the bubble behavior from a drag-buoyancy description of the flow [19,20]. For bubble evolution in the steady state, drag and buoyancy forces on the bubble balance each other giving

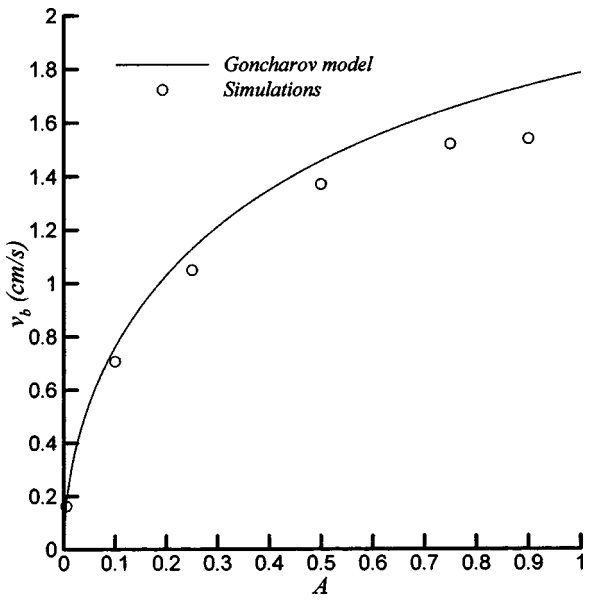

FIG. 8. The z-averaged bulk bubble vertical velocity from the simulations, compared with the Goncharov model.

$$(\rho_2-\rho_1)g=\frac{C_d}{\lambda}\rho_2 v_b^2. \tag{17}$$

Oron *et al.* [20] suggest taking $C_d=2\pi$, giving v_b identical to Eq. (3). A similar argument applied to the spikes gives

$$v_s\sim\sqrt{\frac{2A}{1-Ak}\frac{g}{}}, \tag{18}$$

which is unbounded for $A\to 1$, denoting the free-fall behavior of spikes.

We note the simulations of Li, Jin, and Glimm [31] who obtain $v_{\mathrm{scl},b}$ largely independent of A, in contrast to our results. However, their simulations were confined to $A>0.5$, where the sensitivity to density ratios is small (only one of their simulations was at $A=0.33$, reporting a value of $v_{\mathrm{scl},b}\sim 0.56$). Li [32] reports a higher value of $v_{\mathrm{scl},b}=0.63$ at $A=0.33$, in closer agreement with our results, while He *et al.* [33] obtain $v_{\mathrm{scl},b}=0.61$ and 0.6 at $A=0.5$ and 0.9, respectively. One may also infer a scaled bubble velocity from the merger simulations of Li [26] for the case where the diameter ratio of adjacent bubbles is close to unity, so that they behave effectively as a periodic array. Then, we obtain for $A=0.67$, $v_{\mathrm{scl},b}=0.37$ from one of Li's simulations. The low Atwood number ($A=0$) simulation of [34] gives $v_{\mathrm{scl},b}=0.75$, in good agreement with our results. Note that Dimonte *et al.* [27] also reported values of $v_{\mathrm{scl},b}$ at $A=0.5$ for a single-mode flow from different benchmark codes commonly used in the study of RT in stabilities. The scaled bubble velocities from [27] were determined to be 0.62 ± 0.03.

The time histories of spike velocities for different Atwood numbers are shown in Fig. 9(a), and show a gradual increase for $A\geqslant 0.5$. Based on 2D simulations, Daly [35] suggested that the bubble diameter increases with A according to $D_b=\lambda_b(1+A)/2$. Spikes which are narrower at high A have greater velocities from mass conservation. At infinite density

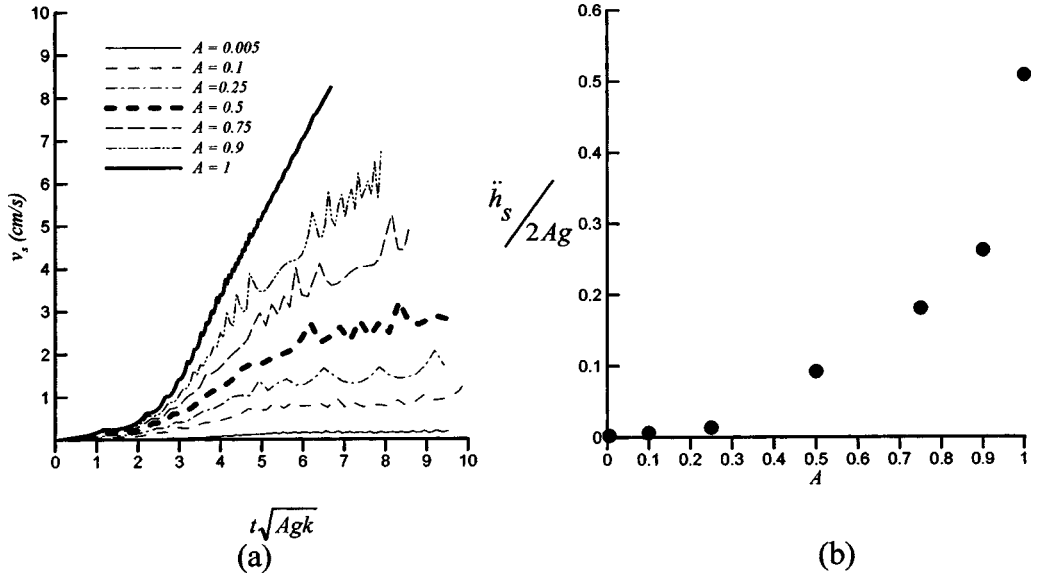

FIG. 9. (a) Spike velocities v_s vs $t\sqrt{Agk}$ at different Atwood numbers showing acceleration for $A \geqslant 0.5$. (b) The corresponding spike acceleration rate for different A.

ratios, the spikes exhibit free-fall behavior $(h_s = \frac{1}{2}gt^2)$. The corresponding nondimensional acceleration rates $(\ddot{h}_s/2Ag)$ are shown in Fig. 9(b), and approach 0.5 at $A=1$, indicating free fall. We note that this tendency toward free-fall behavior has been observed elsewhere, in the simulations of He *et al.* [33], whose spike acceleration rates correspond to $\ddot{h}_s/2Ag = 0.36$ at $A=0.9$.

The scaled spike velocities $v_{\mathrm{scl},s}$ (Fig. 10) also show a dependence on A, in agreement with [17,19]. The spike velocities were determined using a procedure similar to that applied to the bubbles described above. At infinite density ratios, the $v_{\mathrm{scl},s}$ from the model becomes unbounded, because the spikes experience free fall, giving $h_s \propto t^2$. In Fig. 10, only the cases with $A \leqslant 0.5$ are shown, since the spike velocities are no longer constant at Atwood numbers above this value.

The convergence properties of bubble and spike velocities at different Atwood numbers are shown in Figs. 11(a) and

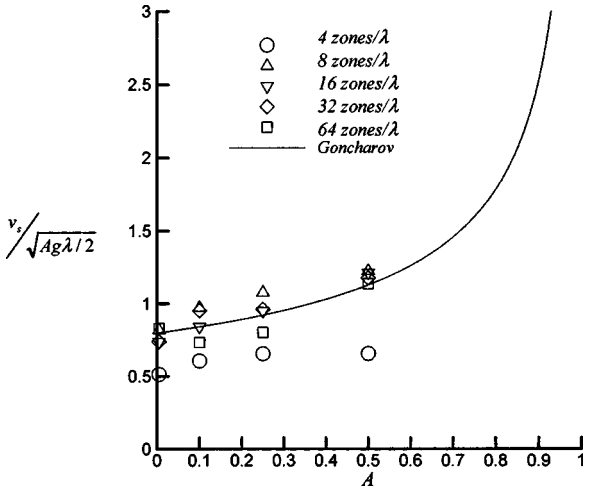

FIG. 10. The scaled spike $(v_s/\sqrt{Ag\lambda/2})$ velocities as a function of A for different zoning.

11(b), respectively. The grid spacing Δ is normalized by the wave number k of the imposed perturbation. Bubbles are better resolved at higher values of A, because they grow to a much larger diameter. For instance, at $A=1$, the convergence curve is almost flat, and the bubble velocity is resolved for all the zone widths except the largest. The converse is true for spike velocities: At higher density differences, the spikes are narrower and are under-resolved for $k\Delta > 0.4$. Zoning studies associated with numerical simulations must account for the variation of bubble and spike velocities with the density difference. In the linear stage, as seen in Fig. 3(b), the convergence of the growth rates is not a function of A, since the heavy and light fluids behave identically. However, the convergence criterion for the linear growth stage of the RT instability is more severe than for the nonlinear stage.

Figure 12 shows the bubble fronts $Z_b(x,y)$ at $A=0.1$ and 0.9, identified as the 50% isosurface of volume fraction. From the figure, it appears that for $r/\lambda \gg 1$, the bubble fronts resemble a sphere rather than a parabola $[z=\zeta_0(t)+\zeta_2 r^2]$ as suggested by the potential flow models. The dash-dotted line shows a sphere with a curvature of $\zeta_2 \sim -k/6.7 = -0.09$ [17], for comparison. The radius of curvature was obtained by fitting a sphere to the bubble surface by considering points located within a distance of $\lambda/8$ from the center, using a least-squares technique (the procedure was repeated by including points in the $0 < r < \lambda/4$ region with nearly identical results). A parabolic fit was also performed using a least-squares technique, and for the region $Z_b \geqslant h_b/2$.

ζ_2 is used by Goncharov and Sohn to describe the shape of the interface between the fluids of different densities; they both predict a constant value independent of A. In good agreement with Goncharov and the 3D simulations of Oparin and Abarzhi [36] at $A=0.82$, Fig. 13 shows $\zeta_2 \sim -k/6.7$ from a spherical fit, independent of A, upon saturation. The parabolic fit does not perform as well, and gives lower values for ζ_2 than the above-mentioned models. Abarzhi *et al.* [22] stipulate that the curvature varies with A at low density dif-

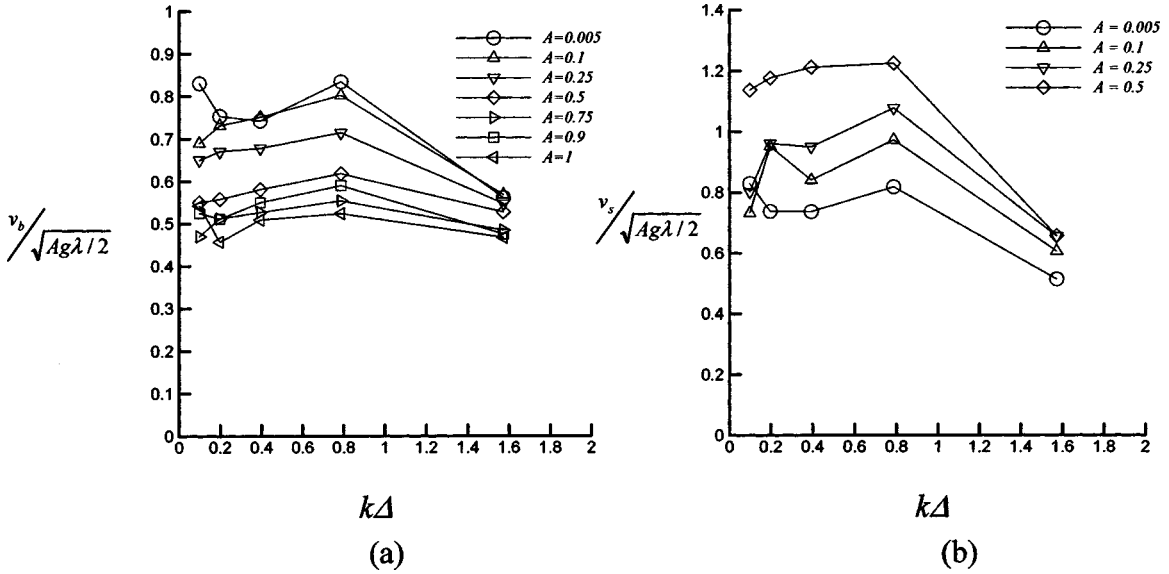

FIG. 11. Convergence of the bubble (a) and spike (b) scaled velocities for different A.

ferences. Neither the spherical nor the parabolic fit shows such a trend.

IV. SUMMARY AND DISCUSSION

In conclusion, the scaled velocities of bubbles were found to depend on the density ratio of RT flows, while the Froude numbers defined by Eq. (5) show no such dependence, in agreement with a recently proposed model based on potential flow theory [17] and previous drag-buoyancy models [19,20]. This picture is complicated in our simulations by the presence of vortices at the bubble-spike interface at low A, which vary the bubble cross section and hence the vertical velocity as a consequence of mass conservation. However, a suitable bulk bubble velocity may be obtained by averaging out area variations of the bubble, giving v_{bulk} in agreement with the potential flow model of Goncharov. The bubble curvature, a critical parameter in all these models, is independent of the Atwood number, in contrast to [22], which suggests variations at low density differences. At low A, spike velocities agree with the results of [17,19,20], and make a continuous transition to free-fall behavior at high A. Ultimately at $A=1$, spikes are in free fall, characterized by a penetration distance that grows as $\frac{1}{2}gt^2$.

The bubble behavior reported here suggests that the growth constant for turbulent RT flow, α_b, decreases slightly with increasing A, according to Dimonte [8] who considered the possibility of a Froude number that behaved according to

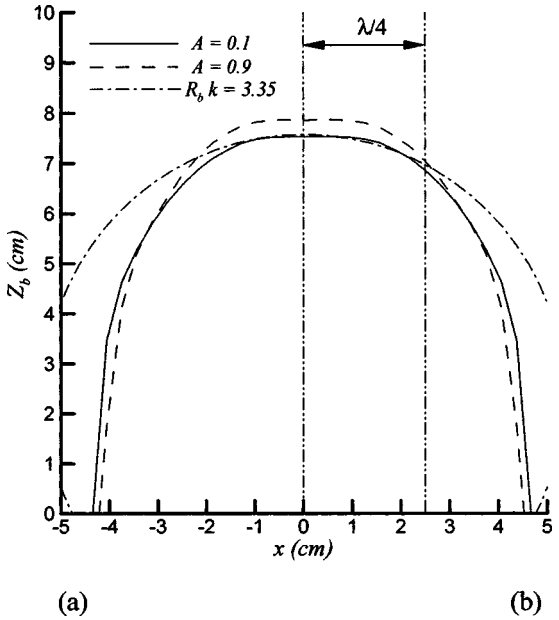

FIG. 12. Bubble front profiles $Z_b(x,y)$ from the $A=0.1$ and 0.9 cases. The theoretical bubble curvature of $R_b k=3.35$ from [17] is shown for comparison.

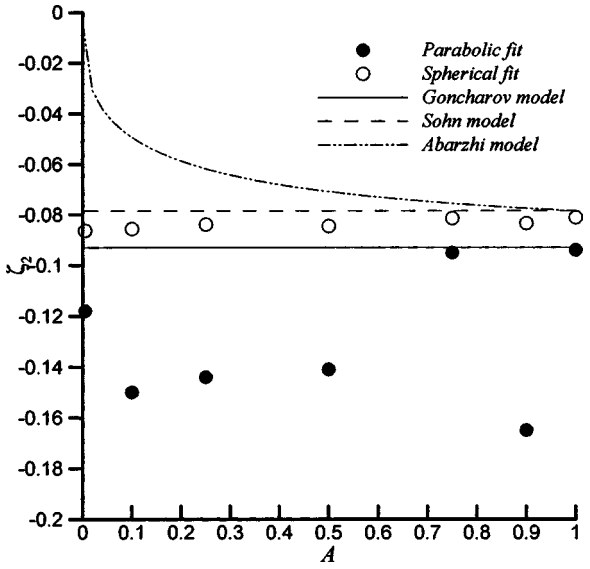

FIG. 13. Bubble curvature from simulations (using parabolic and spherical fits) and from potential flow models.

Goncharov's model [17]. Dimonte [8] further showed that α_b decreases by 25% as the Atwood number is varied from 0 to 1. Measurements from linear electric motor experiments [37] support this claim although the α_b value recovers slightly at very high density differences, possibly due to surface-tension effects. We believe high resolution numerical simulations of the multimode RT flow at different Atwood numbers would be helpful in further understanding these issues.

While our results presented here would be helpful in developing turbulence models based on single-mode dynamics of bubbles, there are some outstanding issues that must be addressed before such models can be improved. One such issue is the observed higher values of Froude number (Fr ~ 1) of bubbles in a chaotic bubble front, resembling the isolated plumes in Scorer's experiment [21]. This is because leading bubbles in a turbulent RT flow would experience less counterflow drag (from mass conservation), resulting in a greater bubble velocity and Froude number. Experiments and numerical simulations similar to those reported here, of isolated plumes as a function of the density ratio could shed light on turbulent RT bubble behavior.

The convergence rates of bubble and spike growth rates in the nonlinear regime depend on the density ratio because of changes in the relative size of bubbles and spikes: For instance at high A, bubbles are large and over-resolved, while the asymptotic spike structures are under-resolved. Consequently, bubble velocities converge faster at higher density ratios, while the converse holds true for spikes. Convergence studies of RT flow should account for the Atwood dependence of bubble and spike behavior.

Finally, the implications of these results extend to bubble merger and competition models, models that characterize the role of initial conditions, and 'mix' models of RT flows. Similar studies of Richtmeyer-Meshkov (RM) flows should also be pursued. Many of the potential flow models discussed here have already been extended to RM flow, and await experimental or numerical verification. Furthermore, the behavior of isolated bubbles and bubble-bubble interaction as a function of the Atwood number should be investigated.

ACKNOWLEDGMENTS

We would like to thank Karnig Mikaelian, Valeri Goncharov, and S. I. Abarzhi for valuable conversations. We thank Malcolm J. Andrews for permitting use of his computer program. This work was performed under the auspices of the U.S. Department of Energy (DOE) by Los Alamos National Laboratory under Contract No. W-7405-ENG-36.

[1] Lord Rayleigh, *Scientific Papers II* (Cambridge University Press, Cambridge, England, 1900).
[2] G. I. Taylor, Proc. R. Soc. London, Ser. A **201**, 192 (1950).
[3] S. F. Gull, Mon. Not. R. Astron. Soc. **171**, 263 (1975).
[4] J. D. Lindl, *Inertial Confinement Fusion: The Quest for Ignition and Energy Gain Using Indirect Drive* (AIP, Woodbury, NY, 1998).
[5] S. Chandrasekhar, *Hydrodynamic and Hydromagnetic Stability* (Oxford University Press, Oxford, 1961).
[6] J. Glimm and X. L. Li, Phys. Fluids **31**, 2077 (1988).
[7] D. Shvarts, U. Alon, D. Ofer, R. L. McCrory, and C. P. Verdon, Phys. Plasmas **2**, 2465 (1995).
[8] Guy Dimonte, Phys. Rev. E **69**, 056305 (2004).
[9] G. Birkhoff, University of California Report No. LA-1862, 1955 (unpublished).
[10] R. M. Davies and G. I. Taylor, Proc. R. Soc. London, Ser. A **200**, 375 (1950).
[11] D. Layzer, Astrophys. J. **122**, 1 (1955).
[12] K. O. Mikaelian, Phys. Rev. E **67**, 026319 (2003).
[13] R. Collins, J. Fluid Mech. **28**, 97 (1967).
[14] Q. Zhang, Phys. Rev. Lett. **81**, 3391 (1998).
[15] J. Hecht, U. Alon, and D. Shvarts, Phys. Fluids **6**, 4019 (1994).
[16] J. Hecht, D. Ofer, U. Alon, D. Shvarts, S. A. Orszag, and R. L. McCrory, Laser Part. Beams **13**, 423 (1995).
[17] V. N. Goncharov, Phys. Rev. Lett. **88**, 134502 (2002).
[18] S-I. Sohn, Phys. Rev. E **67**, 026301 (2003).
[19] U. Alon, J. Hecht, D. Ofer, and D. Shvarts, Phys. Rev. Lett. **74**, 534 (1995).
[20] D. Oron *et al.*, Phys. Plasmas **8**, 2883 (2001).
[21] R. S. Scorer, J. Fluid Mech. **2**, 583 (1957).
[22] S. I. Abarzhi, K. Nishihara, and J. Glimm, Phys. Lett. A **317**, 470 (2003).
[23] M. J. Andrews, Int. J. Numer. Methods Fluids **21**, 205 (1995).
[24] B. Van Leer, J. Comput. Phys. **23**, 276 (1977).
[25] D. L. Youngs, in Proceedings of 16th AIAA Computational Fluid Dynamics Conference, 2003, AIAA Report No. 2003-4102 (unpublished).
[26] X. L. Li, Phys. Fluids **8**, 336 (1996).
[27] Guy Dimonte *et al.*, Phys. Fluids **16**, 1668 (2004).
[28] P. Ramaprabhu, Guy Dimonte, and M. J. Andrews (unpublished).
[29] S. I. Abarzhi (private communication).
[30] V. N. Goncharov (private communication).
[31] X. L. Li, B. X. Jin, and J. Glimm, J. Comput. Phys. **126**, 343 (1996).
[32] X. L. Li, Phys. Fluids A **5**, 1904 (1993).
[33] X. He *et al.*, Phys. Fluids **11**, 1143 (1999).
[34] G. Tryggvason and S. O. Unverdi, Phys. Fluids A **2**, 656 (1990).
[35] B. J. Daly, Phys. Fluids **10**, 297 (1967).
[36] A. Oparin and S. Abarzhi, Phys. Fluids **11**, 3306 (1999).
[37] Guy Dimonte and M. Schneider, Phys. Fluids **12**, 304 (2000); M. Schneider, Guy Dimonte, and B. Remington, Phys. Rev. Lett. **80**, 3507 (1998).